

Study of $B^0 \rightarrow \bar{D}^{(*)0} \pi^+ \pi^-$ decays

K. Abe,¹⁰ K. Abe,⁴⁶ N. Abe,⁴⁹ I. Adachi,¹⁰ H. Aihara,⁴⁸ M. Akatsu,²⁴ Y. Asano,⁵³
 T. Aso,⁵² V. Aulchenko,² T. Aushev,¹⁴ T. Aziz,⁴⁴ S. Bahinipati,⁶ A. M. Bakich,⁴³
 Y. Ban,³⁶ M. Barbero,⁹ A. Bay,²⁰ I. Bedny,² U. Bitenc,¹⁵ I. Bizjak,¹⁵ S. Blyth,²⁹
 A. Bondar,² A. Bozek,³⁰ M. Bračko,^{22,15} J. Brodzicka,³⁰ T. E. Browder,⁹ M.-C. Chang,²⁹
 P. Chang,²⁹ Y. Chao,²⁹ A. Chen,²⁶ K.-F. Chen,²⁹ W. T. Chen,²⁶ B. G. Cheon,⁴
 R. Chistov,¹⁴ S.-K. Choi,⁸ Y. Choi,⁴² Y. K. Choi,⁴² A. Chuvikov,³⁷ S. Cole,⁴³
 M. Danilov,¹⁴ M. Dash,⁵⁵ L. Y. Dong,¹² R. Dowd,²³ J. Dragic,²³ A. Drutskoy,⁶
 S. Eidelman,² Y. Enari,²⁴ D. Epifanov,² C. W. Everton,²³ F. Fang,⁹ S. Fratina,¹⁵
 H. Fujii,¹⁰ N. Gabyshev,² A. Garmash,³⁷ T. Gershon,¹⁰ A. Go,²⁶ G. Gokhroo,⁴⁴
 B. Golob,^{21,15} M. Grosse Perdekamp,³⁸ H. Guler,⁹ J. Haba,¹⁰ F. Handa,⁴⁷ K. Hara,¹⁰
 T. Hara,³⁴ N. C. Hastings,¹⁰ K. Hasuko,³⁸ K. Hayasaka,²⁴ H. Hayashii,²⁵ M. Hazumi,¹⁰
 E. M. Heenan,²³ I. Higuchi,⁴⁷ T. Higuchi,¹⁰ L. Hinz,²⁰ T. Hojo,³⁴ T. Hokuue,²⁴
 Y. Hoshi,⁴⁶ K. Hoshina,⁵¹ S. Hou,²⁶ W.-S. Hou,²⁹ Y. B. Hsiung,²⁹ H.-C. Huang,²⁹
 T. Igaki,²⁴ Y. Igarashi,¹⁰ T. Iijima,²⁴ A. Imoto,²⁵ K. Inami,²⁴ A. Ishikawa,¹⁰ H. Ishino,⁴⁹
 K. Itoh,⁴⁸ R. Itoh,¹⁰ M. Iwamoto,³ M. Iwasaki,⁴⁸ Y. Iwasaki,¹⁰ R. Kagan,¹⁴ H. Kakuno,⁴⁸
 J. H. Kang,⁵⁶ J. S. Kang,¹⁷ P. Kapusta,³⁰ S. U. Kataoka,²⁵ N. Katayama,¹⁰ H. Kawai,³
 H. Kawai,⁴⁸ Y. Kawakami,²⁴ N. Kawamura,¹ T. Kawasaki,³² N. Kent,⁹ H. R. Khan,⁴⁹
 A. Kibayashi,⁴⁹ H. Kichimi,¹⁰ H. J. Kim,¹⁹ H. O. Kim,⁴² Hyunwoo Kim,¹⁷ J. H. Kim,⁴²
 S. K. Kim,⁴¹ T. H. Kim,⁵⁶ K. Kinoshita,⁶ P. Koppenburg,¹⁰ S. Korpar,^{22,15} P. Krizán,^{21,15}
 P. Krokovny,² R. Kulasiri,⁶ C. C. Kuo,²⁶ H. Kurashiro,⁴⁹ E. Kurihara,³ A. Kusaka,⁴⁸
 A. Kuzmin,² Y.-J. Kwon,⁵⁶ J. S. Lange,⁷ G. Leder,¹³ S. E. Lee,⁴¹ S. H. Lee,⁴¹
 Y.-J. Lee,²⁹ T. Lesiak,³⁰ J. Li,⁴⁰ A. Limosani,²³ S.-W. Lin,²⁹ D. Liventsev,¹⁴
 J. MacNaughton,¹³ G. Majumder,⁴⁴ F. Mandl,¹³ D. Marlow,³⁷ T. Matsuishi,²⁴
 H. Matsumoto,³² S. Matsumoto,⁵ T. Matsumoto,⁵⁰ A. Matyja,³⁰ Y. Mikami,⁴⁷
 W. Mitaroff,¹³ K. Miyabayashi,²⁵ Y. Miyabayashi,²⁴ H. Miyake,³⁴ H. Miyata,³² R. Mizuk,¹⁴
 D. Mohapatra,⁵⁵ G. R. Moloney,²³ G. F. Moorhead,²³ T. Mori,⁴⁹ A. Murakami,³⁹
 T. Nagamine,⁴⁷ Y. Nagasaka,¹¹ T. Nakadaira,⁴⁸ I. Nakamura,¹⁰ E. Nakano,³³ M. Nakao,¹⁰
 H. Nakazawa,¹⁰ Z. Natkaniec,³⁰ K. Neichi,⁴⁶ S. Nishida,¹⁰ O. Nitoh,⁵¹ S. Noguchi,²⁵
 T. Nozaki,¹⁰ A. Ogawa,³⁸ S. Ogawa,⁴⁵ T. Ohshima,²⁴ T. Okabe,²⁴ S. Okuno,¹⁶
 S. L. Olsen,⁹ Y. Onuki,³² W. Ostrowicz,³⁰ H. Ozaki,¹⁰ P. Pakhlov,¹⁴ H. Palka,³⁰
 C. W. Park,⁴² H. Park,¹⁹ K. S. Park,⁴² N. Parslow,⁴³ L. S. Peak,⁴³ M. Pernicka,¹³
 J.-P. Perroud,²⁰ M. Peters,⁹ L. E. Piilonen,⁵⁵ A. Poluektov,² F. J. Ronga,¹⁰ N. Root,²
 M. Rozanska,³⁰ H. Sagawa,¹⁰ M. Saigo,⁴⁷ S. Saitoh,¹⁰ Y. Sakai,¹⁰ H. Sakamoto,¹⁸
 T. R. Sarangi,¹⁰ M. Satapathy,⁵⁴ N. Sato,²⁴ O. Schneider,²⁰ J. Schümann,²⁹ C. Schwanda,¹³
 A. J. Schwartz,⁶ T. Seki,⁵⁰ S. Semenov,¹⁴ K. Senyo,²⁴ Y. Settai,⁵ R. Seuster,⁹
 M. E. Sevier,²³ T. Shibata,³² H. Shibuya,⁴⁵ B. Shwartz,² V. Sidorov,² V. Siegle,³⁸
 J. B. Singh,³⁵ A. Somov,⁶ N. Soni,³⁵ R. Stamen,¹⁰ S. Stanič,^{53,*} M. Starič,¹⁵ A. Sugi,²⁴
 A. Sugiyama,³⁹ K. Sumisawa,³⁴ T. Sumiyoshi,⁵⁰ S. Suzuki,³⁹ S. Y. Suzuki,¹⁰ O. Tajima,¹⁰
 F. Takasaki,¹⁰ K. Tamai,¹⁰ N. Tamura,³² K. Tanabe,⁴⁸ M. Tanaka,¹⁰ G. N. Taylor,²³
 Y. Teramoto,³³ X. C. Tian,³⁶ S. Tokuda,²⁴ S. N. Tovey,²³ K. Trabelsi,⁹ T. Tsuboyama,¹⁰

T. Tsukamoto,¹⁰ K. Uchida,⁹ S. Uehara,¹⁰ T. Uglov,¹⁴ K. Ueno,²⁹ Y. Unno,³ S. Uno,¹⁰
Y. Ushiroda,¹⁰ G. Varner,⁹ K. E. Varvell,⁴³ S. Villa,²⁰ C. C. Wang,²⁹ C. H. Wang,²⁸
J. G. Wang,⁵⁵ M.-Z. Wang,²⁹ M. Watanabe,³² Y. Watanabe,⁴⁹ L. Widhalm,¹³
Q. L. Xie,¹² B. D. Yabsley,⁵⁵ A. Yamaguchi,⁴⁷ H. Yamamoto,⁴⁷ S. Yamamoto,⁵⁰
T. Yamanaka,³⁴ Y. Yamashita,³¹ M. Yamauchi,¹⁰ Heyoung Yang,⁴¹ P. Yeh,²⁹ J. Ying,³⁶
K. Yoshida,²⁴ Y. Yuan,¹² Y. Yusa,⁴⁷ H. Yuta,¹ S. L. Zang,¹² C. C. Zhang,¹² J. Zhang,¹⁰
L. M. Zhang,⁴⁰ Z. P. Zhang,⁴⁰ V. Zhilich,² T. Ziegler,³⁷ D. Žontar,^{21,15} and D. Zürcher²⁰

(Belle Collaboration)

¹*Aomori University, Aomori*

²*Budker Institute of Nuclear Physics, Novosibirsk*

³*Chiba University, Chiba*

⁴*Chonnam National University, Kwangju*

⁵*Chuo University, Tokyo*

⁶*University of Cincinnati, Cincinnati, Ohio 45221*

⁷*University of Frankfurt, Frankfurt*

⁸*Gyeongsang National University, Chinju*

⁹*University of Hawaii, Honolulu, Hawaii 96822*

¹⁰*High Energy Accelerator Research Organization (KEK), Tsukuba*

¹¹*Hiroshima Institute of Technology, Hiroshima*

¹²*Institute of High Energy Physics,*

Chinese Academy of Sciences, Beijing

¹³*Institute of High Energy Physics, Vienna*

¹⁴*Institute for Theoretical and Experimental Physics, Moscow*

¹⁵*J. Stefan Institute, Ljubljana*

¹⁶*Kanagawa University, Yokohama*

¹⁷*Korea University, Seoul*

¹⁸*Kyoto University, Kyoto*

¹⁹*Kyungpook National University, Taegu*

²⁰*Swiss Federal Institute of Technology of Lausanne, EPFL, Lausanne*

²¹*University of Ljubljana, Ljubljana*

²²*University of Maribor, Maribor*

²³*University of Melbourne, Victoria*

²⁴*Nagoya University, Nagoya*

²⁵*Nara Women's University, Nara*

²⁶*National Central University, Chung-li*

²⁷*National Kaohsiung Normal University, Kaohsiung*

²⁸*National United University, Miao Li*

²⁹*Department of Physics, National Taiwan University, Taipei*

³⁰*H. Niewodniczanski Institute of Nuclear Physics, Krakow*

³¹*Nihon Dental College, Niigata*

³²*Niigata University, Niigata*

³³*Osaka City University, Osaka*

³⁴*Osaka University, Osaka*

³⁵*Panjab University, Chandigarh*

³⁶*Peking University, Beijing*

³⁷*Princeton University, Princeton, New Jersey 08545*

³⁸*RIKEN BNL Research Center, Upton, New York 11973*

³⁹*Saga University, Saga*

⁴⁰*University of Science and Technology of China, Hefei*

⁴¹*Seoul National University, Seoul*

⁴²*Sungkyunkwan University, Suwon*

⁴³*University of Sydney, Sydney NSW*

⁴⁴*Tata Institute of Fundamental Research, Bombay*

⁴⁵*Toho University, Funabashi*

⁴⁶*Tohoku Gakuin University, Tagajo*

⁴⁷*Tohoku University, Sendai*

⁴⁸*Department of Physics, University of Tokyo, Tokyo*

⁴⁹*Tokyo Institute of Technology, Tokyo*

⁵⁰*Tokyo Metropolitan University, Tokyo*

⁵¹*Tokyo University of Agriculture and Technology, Tokyo*

⁵²*Toyama National College of Maritime Technology, Toyama*

⁵³*University of Tsukuba, Tsukuba*

⁵⁴*Utkal University, Bhubaneswer*

⁵⁵*Virginia Polytechnic Institute and State University, Blacksburg, Virginia 24061*

⁵⁶*Yonsei University, Seoul*

Abstract

We report the results of a study of neutral B decays to the $D^0\pi^+\pi^-$ and $D^{*0}\pi^+\pi^-$ final states using complete $D^{(*)0}$ reconstruction. The contributions from two-body $B \rightarrow D^{**}\pi$ with narrow ($j_q = 3/2$) D^{**} states and $B \rightarrow D^{(*)}\rho, D^{(*)}f_2, D^{(*)}\sigma$ decays have been determined. All results are preliminary, and are based on a large data sample collected in the Belle experiment at the KEKB e^+e^- collider.

PACS numbers: 13.25.Hw, 14.40.Lb, 14.40.Nd

The decays of B meson to $D\pi$ and $D^*\pi$ final states are two of its dominant hadronic decay modes and have been measured quite well [1]. In this paper we study the production of excited states of D -mesons, collectively referred to as D^{**} 's, that are P-wave excitations of quark-antiquark systems containing one charmed and one light (u, d) quark. The results provide tests of Heavy Quark Effective Theory (HQET) and QCD sum rules. Figure 1 shows the spectrum of D -meson excitations. In the heavy quark limit, the heavy quark spin \vec{s}_c decouples from the other degrees of freedom and the total angular momentum of the light quark $\vec{j}_q = \vec{L} + \vec{s}_q$ is a good quantum number. There are four P-wave states with the following spin-parity and light quark angular momenta: $0^+(j_q = 1/2)$, $1^+(j_q = 1/2)$, $1^+(j_q = 3/2)$ and $2^+(j_q = 3/2)$, which are usually labeled as D_0^* , D_1' , D_1 and D_2^* , respectively.

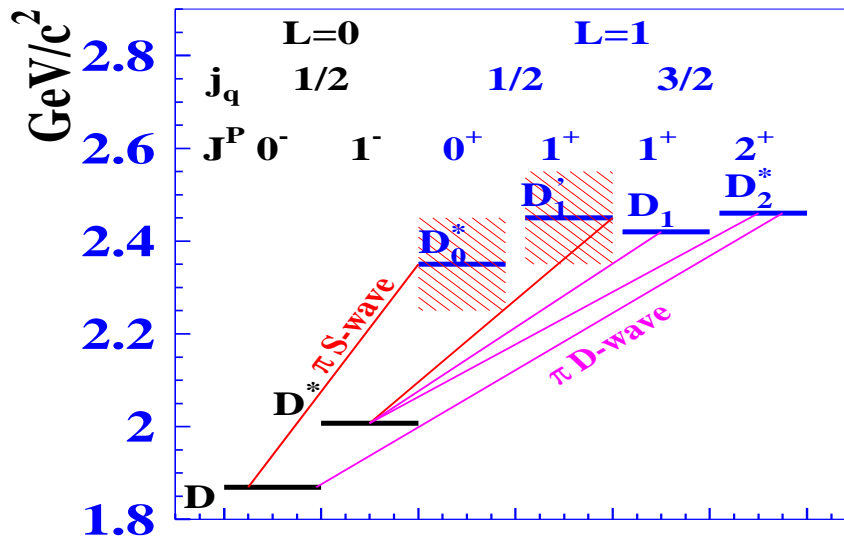


FIG. 1: Spectrum of D-meson excitations. Lines show possible one pion transitions.

The two $j_q = 3/2$ states are narrow with widths of about 20-40 MeV and were previously observed [2, 3, 4, 5, 6, 7, 8, 9, 10, 11, 12]. The measured values of their masses agree with model predictions [13, 14, 15, 16]. The remaining $j_q = 1/2$ states decay via S-waves and are expected to be quite broad.

The $B \rightarrow D^{(*)}\pi\pi$ decay provides a possibility to study D^{**} production. The fixed spin of the initial state makes it possible to perform an angular analysis of the decay products and to separate final states with different quantum numbers.

We have acquired a large sample of B decays using the Belle detector, which has good resolution and particle ID. These data can be used to contribute to an understanding of these problems.

Earlier neutral D^{**} production in charged B -decays has been studied at Belle [17]. All four D^{**} states have been observed and the production rate of the broad ($j = 1/2$)-states appears to be comparable to that of the narrow ($j = 3/2$)-states. This work describes a similar analysis of the decay $\bar{B}^0 \rightarrow D^{**+}\pi^-$.

In the case of neutral B decay the $D^{(*)}\pi\pi$ final state contains two pions of opposite sign that can form several bound states (such as ρ , f_0 , f_2), which should also be taken into account. The presence of $\pi\pi$ bound states complicates the analysis but can give valuable information about the constants and mechanism of these decays.

THE BELLE DETECTOR

The Belle detector [18] is a large-solid-angle magnetic spectrometer that consists of a three-layer silicon vertex detector (SVD), a 50-layer central drift chamber (CDC) for charged particle tracking and specific ionization measurement (dE/dx), an array of aerogel threshold Čerenkov counters (ACC), time-of-flight scintillation counters (TOF), and an array of 8736 CsI(Tl) crystals for electromagnetic calorimetry (ECL) located inside a superconducting solenoid coil that provides a 1.5 T magnetic field. An iron flux return located outside the coil is instrumented to detect K_L mesons and identify muons (KLM). We use a GEANT-based Monte Carlo (MC) simulation to model the response of the detector and to determine its acceptance [19].

Separation of kaons and pions is accomplished by combining the responses of the ACC and the TOF with dE/dx measurements in the CDC to form a likelihood $\mathcal{L}(h)$ where $h = (\pi)$ or (K) . Charged particles are identified as pions or kaons using the likelihood ratio (\mathcal{R}):

$$\mathcal{R}(K) = \frac{\mathcal{L}(K)}{\mathcal{L}(K) + \mathcal{L}(\pi)}; \quad \mathcal{R}(\pi) = \frac{\mathcal{L}(\pi)}{\mathcal{L}(K) + \mathcal{L}(\pi)} = 1 - \mathcal{R}(K).$$

At large momenta (>2.5 GeV/ c) only the ACC and dE/dx are used since the TOF provides no significant separation of kaons and pions. Electron identification is based on a combination of dE/dx measurements, ACC photoelectron yields and the position, shape and total energy deposition (E/p) of the shower detected in the ECL. A more detailed description of the Belle particle identification can be found in Ref. [20].

EVENT SELECTION

A data sample of 140 fb^{-1} (152 million $B\bar{B}$ events) collected at the $\Upsilon(4S)$ resonance with the Belle detector is used. Candidate $\bar{B}^0 \rightarrow D^0\pi^+\pi^-$ and $\bar{B}^0 \rightarrow D^{*0}\pi^+\pi^-$ events as well as charge conjugate combinations are selected. The D^0 and D^{*0} mesons are reconstructed in $D^0 \rightarrow K^-\pi^+$ and $D^{*0} \rightarrow D^0\pi^0$ modes, respectively. D^0 from D^{*0} decay is detected in channels $D^0 \rightarrow K^-\pi^+$ and $D^0 \rightarrow K^-\pi^+\pi^+\pi^-$. The signal-to-background ratios for other D decay modes are found to be much lower and they are not used in this analysis.

Charged tracks are selected with requirements based on the average hit residuals and impact parameters relative to the interaction point. We also require that the polar angle of each track be within the angular range of $17^\circ - 150^\circ$ and that the transverse track momentum be greater than 50 MeV/ c for kaons and 25 MeV/ c for pions.

Charged kaon candidates are selected with the requirement $\mathcal{R}(K) > 0.6$. This has an efficiency of 90% for kaons and a pion misidentification probability of 10%. For pions the requirement $\mathcal{R}(\pi) > 0.2$ is used. All tracks that are positively identified as electrons are rejected.

D^0 mesons are reconstructed from $K^-\pi^+$ combinations with invariant mass within 12 MeV/ c^2 of the nominal D^0 mass, which corresponds to about $2.5 \sigma_{K\pi}$. We reconstruct D^{*0}

mesons from the $D\pi^0$ combinations with a mass difference of $M_{D\pi^0} - M_{D^0}$ within $2.5 \text{ MeV}/c^2$ of its nominal value.

Candidate events are identified by their center of mass (c.m.) energy difference, $\Delta E = (\sum_i E_i) - E_b$, and beam-constrained mass, $M_{bc} = \sqrt{E_b^2 - (\sum_i \vec{p}_i)^2}$, where $E_b = \sqrt{s}/2$ is the beam energy in the $\Upsilon(4S)$ c.m. frame, and \vec{p}_i and E_i are the c.m. three-momenta and energies of the B meson candidate decay products. We select events with $M_{bc} > 5.25 \text{ GeV}/c^2$ and $|\Delta E| < 0.10 \text{ GeV}$.

To suppress the large continuum background ($e^+e^- \rightarrow q\bar{q}$, where $q = u, d, s, c$), topological variables are used. Since the produced B mesons are almost at rest in the c.m. frame, the angles of the decay products of the two B mesons are uncorrelated and the tracks tend to be isotropic while continuum $q\bar{q}$ events tend to have a two-jet structure. We use the angle between the thrust axis of the B candidate and that of the rest of the event (Θ_{thrust}) to discriminate between these two cases. The distribution of $|\cos \Theta_{\text{thrust}}|$ is strongly peaked near $|\cos \Theta_{\text{thrust}}| = 1$ for $q\bar{q}$ events and is nearly flat for $\Upsilon(4S) \rightarrow B\bar{B}$ events. We require $|\cos \Theta_{\text{thrust}}| < 0.8$, which eliminates about 83% of the continuum background while retaining about 80% of signal events.

There are events for which two or more combinations pass all the selection criteria. According to a MC simulation, this occurs primarily because of the misreconstruction of a low momentum pion from the $D^{**} \rightarrow D^{(*)}\pi$ decay. To avoid multiple entries, the combination that has the minimum difference of Z coordinates at the interaction point, $|Z_{\pi_1} - Z_{\pi_2}|$, of the tracks corresponding to the pions from $B \rightarrow D^{**}\pi_1$ and $D^{**} \rightarrow D^{(*)}\pi_2$ decays is selected [21]. This selection suppresses the combinations that include pions from K_S decays. In the case of multiple D combinations, the one with invariant mass closest to the nominal value is selected.

$\bar{B}^0 \rightarrow D^0\pi^+\pi^-$ ANALYSIS.

The final state of the $\bar{B}^0 \rightarrow D^0\pi^+\pi^-$ decay together with three-body and quasi-two-body events includes the two-body decay $\bar{B}^0 \rightarrow D^{*+}\pi^-$ followed by the decay $D^{*+} \rightarrow D^0\pi^+$. Using the mass difference of $M_{D\pi} - M_D$ we subdivide the total sample in two: events with $|M_{D\pi} - M_D - 0.1455| < 0.03 \text{ (GeV}/c^2)$ ($\sim 6\sigma$) (denoted further as sample (2)) correspond to $D^*\pi$ production and the rest of the events $D\pi\pi$ form sample (1).

The M_{bc} and ΔE distributions for $\bar{B}^0 \rightarrow D^0\pi^+\pi^-$ events are shown in Fig. 2. The distributions are plotted for events that satisfy the selection criteria for the other variable: i.e., $|\Delta E| < 25 \text{ MeV}$ and $|M_{bc} - M_B| < 5 \text{ MeV}/c^2$ for the M_{bc} and the ΔE histograms, respectively. A clear signal is evident in both distributions. The signal yield is obtained by fitting the ΔE distribution to the sum of two Gaussians with the same mean for the signal and a linear function for background. The widths and the relative normalization of the two Gaussians are fixed at values obtained from the MC simulation while the signal normalization as well as the constant term and slope of the background linear function are treated as free parameters.

The signal yields are 1128 ± 51 and 1521 ± 40 for samples (1) and (2), respectively. A detection efficiency of $(16.8 \pm 0.4)\%$ and $(18.2 \pm 0.4)\%$ is determined from a MC simulation that uses a Dalitz plot distribution that is generated according to the model described in the next section. Taking into account the branching fraction $\mathcal{B}(D^0 \rightarrow K^-\pi^+) = (3.80 \pm 0.09)\%$ and $\mathcal{B}(D^{*+} \rightarrow D^0\pi^+) = (67.7 \pm 0.5)\%$ [1], we obtain the following value for the branching

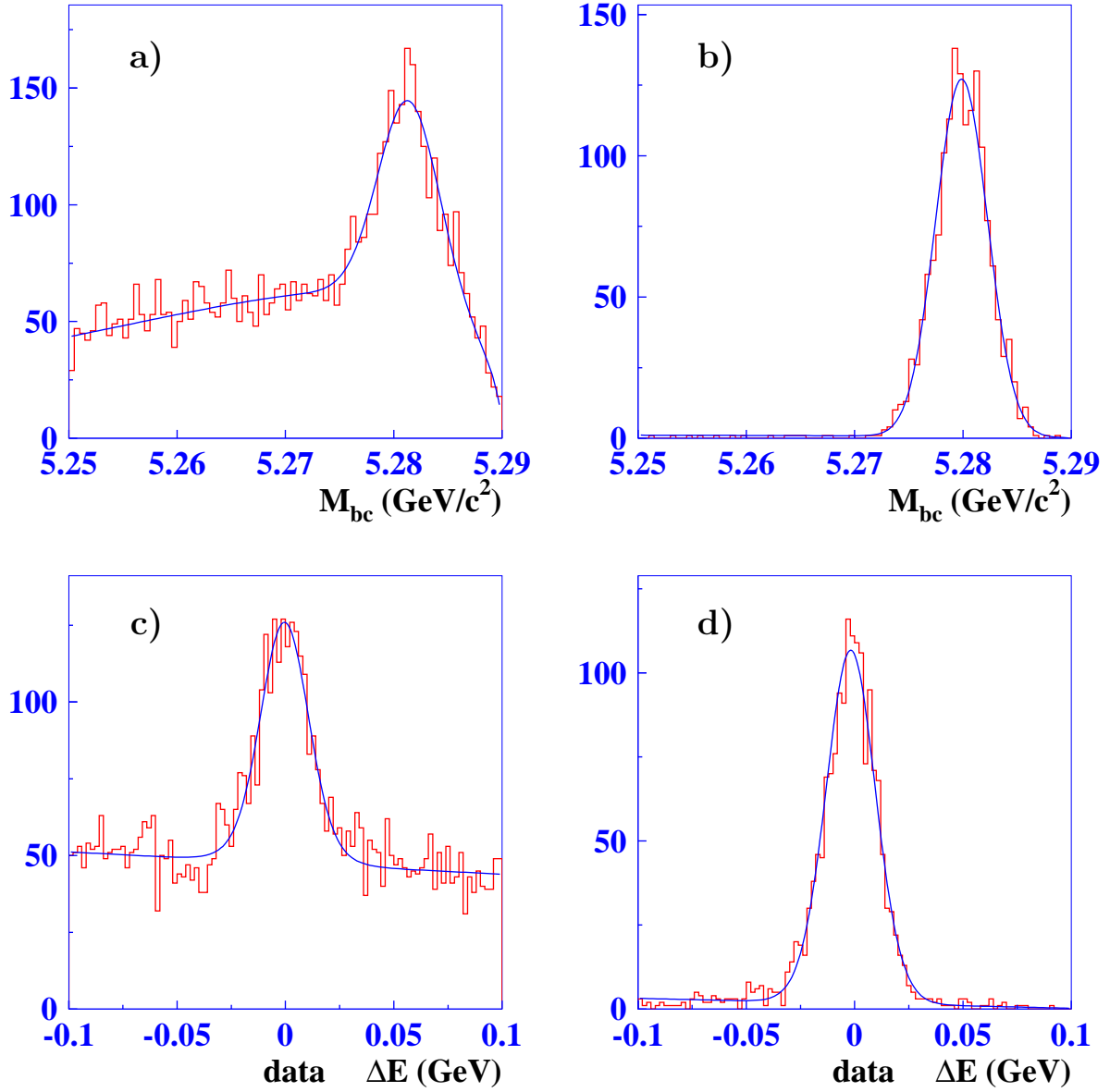


FIG. 2: M_{bc} and ΔE distributions for $\bar{B}^0 \rightarrow D^0 \pi^+ \pi^-$ events. (a),(b) show M_{bc} distributions. (c),(d) show ΔE distributions. (a),(c) ((b),(d)) distributions are plotted for sample (1)((2)), respectively.

fractions:

$$\mathcal{B}(\bar{B}^0 \rightarrow D^0 \pi^+ \pi^-) = (1.07 \pm 0.06 \pm 0.10) \times 10^{-3},$$

and

$$\mathcal{B}(\bar{B}^0 \rightarrow D^{*+} \pi^-) = (2.30 \pm 0.06 \pm 0.19) \times 10^{-3},$$

where the first error is statistical and second error is systematic. The main contributions to the systematic error are listed in Table I. The uncertainty of the background shape was estimated by adding higher order polynomial terms to the approximating function.

Source	$\sigma_{sys}, \%$	
	sample(1)	sample(2)
PID	5%	5%
Background	5%	1%
Tracking	4.4%	5.4%
MC	3%	3%
Br(D, D^*)	2.4%	2.5%
Total	9.2%	8.1%

TABLE I: The systematic uncertainties for $\bar{B}^0 \rightarrow D^0\pi^+\pi^-$.

The values of $\mathcal{B}(\bar{B}^0 \rightarrow D^0\pi^+\pi^-)$ and $\mathcal{B}(\bar{B}^0 \rightarrow D^{*+}\pi^-)$ are in agreement with a previous result from Belle: $\mathcal{B}(\bar{B}^0 \rightarrow D^0\pi^+\pi^-) = (8.0 \pm 1.6) \times 10^{-4}$ [22] and a CLEO result: $\mathcal{B}(\bar{B}^0 \rightarrow D^{*+}\pi^-) = (2.81 \pm 0.25) \times 10^{-4}$ [23] and are more precise.

$B \rightarrow D\pi\pi$ Dalitz plot analysis

For a three-body decay of a spin zero particle, two variables are required to describe the decay kinematics; we use the $D^0\pi^+$ and $\pi^+\pi^-$ invariant masses squared, q^2 and q_1^2 , respectively.

To analyze the dynamics of $B \rightarrow D\pi\pi$ decays, events with ΔE and M_{bc} within the signal region $((\Delta E + \kappa(M_{bc} - M_B))/\sigma_{\Delta E})^2 + ((M_{bc} - M_B)/\sigma_{M_{bc}})^2 < 4$ are selected. The parameters $\sigma_{\Delta E} = 11\text{MeV}/c^2$, $\sigma_{M_{bc}} = 2.7\text{MeV}/c^2$, $\kappa = 0.9$ have been obtained from a fit to experimental data; the coefficient κ takes into account a correlation between M_{bc} and ΔE .

To model the contribution and shape of the background, we use events from the ΔE sidebands, which are defined as: $((\Delta E \pm 65\text{MeV} + \kappa(M_{bc} - M_B))/\sigma_{\Delta E})^2 + ((M_{bc} - M_B)/\sigma_{M_{bc}})^2 < 4$. Figure 3 shows the signal and sidebands regions in the $(M_{bc} - \Delta E)$ plane.

The $D\pi$ and $\pi\pi$ mass distributions for the signal and sideband events are shown in Fig. 4. In the $D\pi$ mass distribution we can clearly see the narrow peak of the D_2^* . The $\pi\pi$ distribution has a signal of the ρ meson as well as a structure at $1.2 - 1.3\text{GeV}/c^2$ that can be due to $f_0(1370)$ or $f_2(1270)$ contributions.

The distributions of events in the $M_{D\pi}^2$ versus $M_{\pi\pi}^2$ Dalitz plot for the signal and sideband regions are shown in Fig. 5. The Dalitz plot boundary is determined by the decay kinematics and the masses of the daughter particles. In order to have the same Dalitz plot boundary for events in both signal and sideband regions, mass-constrained fits of $K\pi$ to M_D and $D\pi\pi$ to M_B are performed. The mass-constrained fits also reduce smearing from detector resolution.

To extract the amplitudes and phases of different intermediate states, an unbinned fit to the Dalitz plot is performed using the method described in Ref. [17]. The event density function in the Dalitz plot is the sum of the signal and background.

The background distribution and normalization are obtained from the ΔE sideband analysis. Since the $D\pi$ mass distributions for the upper and lower halves of the ΔE sideband have similar shapes, we can expect similar background behavior for the signal and sideband regions. The background Dalitz plot has neither a resonant structure nor non-trivial helicity behavior and is combinatorial in its origin. The background shape is obtained from

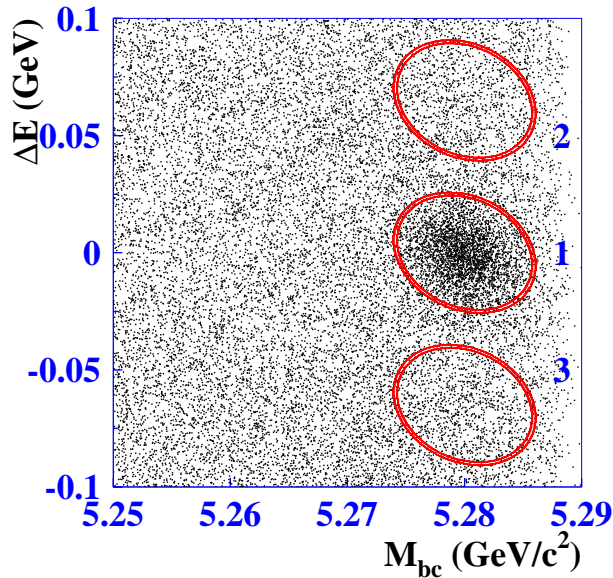


FIG. 3: The experimental event distribution in the $(M_{bc} - \Delta E)$ plot. The ellipses show a position of the signal (1) and sideband regions (2),(3).

an unbinned fit of the sideband distribution to a smooth two-dimensional function. The number of background events in the signal region is scaled according to the relative areas of the signal and the sideband regions.

There is no generally accepted way to exactly describe a three-body amplitude. In this paper we represent the $D\pi\pi$ amplitude as the sum of Breit-Wigner contributions for different intermediate two-body states. Such an approach cannot be exact since it is neither analytic nor unitary and does not take describe completely possible final state interactions. Nevertheless, the sum of Breit-Wigners describes the main features of the amplitude behavior and allows one to find and distinguish the contributions of various two-body intermediate states, their interference and the effective parameters of these states. We used the same approach in the analysis of charged B decays [17].

In the $D^0\pi^+\pi^-$ final state a combination of the D^0 -meson and a pion can form a vector meson D^{*+} , a tensor meson D_2^{*+} or a scalar state D_0^{*+} ; the axial vector mesons D_1^+ and $D_1^{'+}$ cannot decay to two pseudoscalars because of angular momentum and parity conservation. The region of the $D^0\pi^+$ invariant mass corresponding to the D^{*+} is excluded from the fitting by requiring $|M_{D\pi} - M_{D^*}| > 0.01 \text{ GeV}/c^2$ but in B decay a virtual D^{*+} (referred to as D_v^*) can be produced off-shell with $\sqrt{q^2}$ larger than the $D^0\pi^+$ total mass and such a process will contribute to the amplitude. Another virtual hadron that can be produced in this combination is B^{*-} (referred to as B_v^*): $B \rightarrow B_v^*\pi$ and $B_v^* \rightarrow D\pi$. For the mass of B^{*-} as well as the mass and width of D^{*+} , we used the PDG values [1]; the widths of B^{*-} are calculated from the width of the D^{*-} in the HQET approach. In the $\pi\pi$ distribution we can see a ρ meson signal and some evidence of resonances around 1300 MeV, which we describe with the hypothesis of $f_2(1270)$ and $f_0(1370)$ mesons. As it is shown in Table II, the hypothesis of f_2 has the best likelihood value. We also include the scalar resonance $f_0(600)$ with free mass and width.

The contributions from the intermediate states listed above are included in the signal-

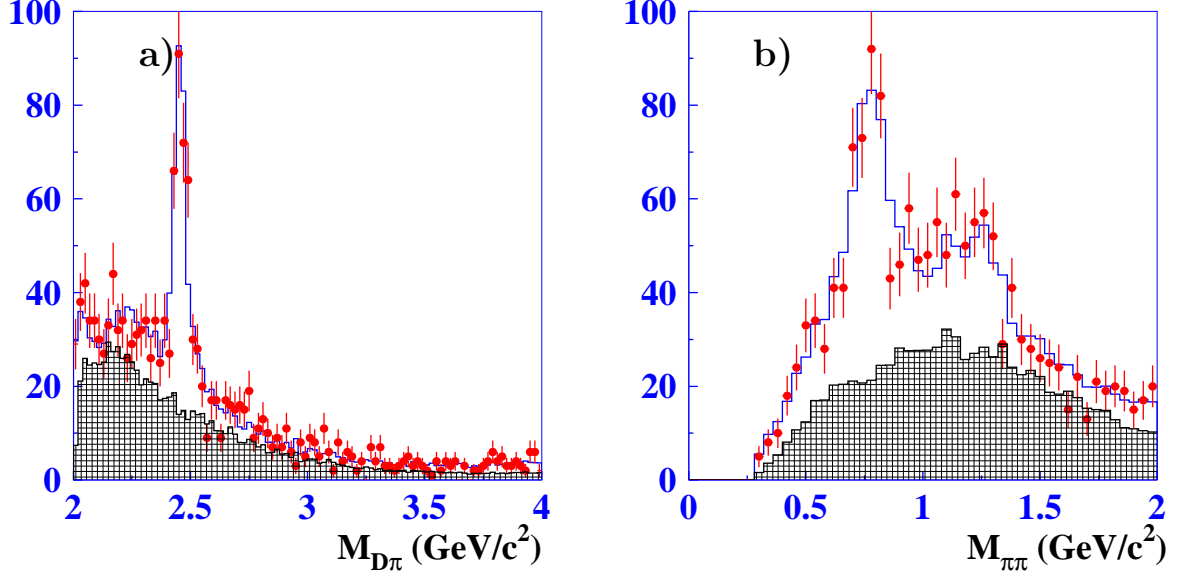


FIG. 4: $D\pi$ - (a) and $\pi\pi$ - (b) mass distribution. The points with error bars correspond to the signal box events, the hatched histogram — to the background obtained from sidebands. The open histogram shows the fit function after efficiency correction.

	$D_2^*, D_v^*, \rho, f_0(600)$						
	D_0^*			$f_2(1270)$			
	$f_2(1270)$	$f_0(1370)$	—	D_0	D_1	D_2	—
$-2 \ln \mathcal{L}/\mathcal{L}_0$	0	49	80	0	-5	16	31

TABLE II: Comparison of the models with different resonances.

event density ($S(q^2, q_1^2)$) parameterization as a coherent sum of the corresponding amplitudes together with a possible constant amplitude (a_{ps}):

$$\begin{aligned}
S(q^2, q_1^2) = & |a_2 A^2(q^2, q_1^2) + a_0 e^{i\phi_0} A^0(q^2, q_1^2) + a_1 e^{i\phi_1} A^1(q^2, q_1^2) \\
& + a_\rho e^{i\phi_\rho} A^\rho + a_{f_0} e^{i(\phi_{f_0} + \phi_\rho)} A^{f_0} + a_{f_2} e^{i(\phi_{f_2} + \phi_\rho)} A^{f_2} \\
& + a_{B^*} e^{i\phi_{B^*}} A^1(q^2, q_1^2) + a_{ps} e^{i\phi_{ps}}|^2.
\end{aligned} \tag{1}$$

Each resonance is described by a relativistic Breit-Wigner with a q^2 dependent width and angular dependence that corresponds to the spins of the intermediate and final state particles following the approach described in [17]. We take into account hadronic transition form factors. The Blatt-Weisskopf parameterization [27] with a hadron scale $r=1.6$ (GeV/c) $^{-1}$ is used. For the virtual mesons D_v^* and B_v^* that are produced beyond the peak region, another form factor parameterization is used:

$$F_{AB}(\mathbf{p}) = e^{-r(\mathbf{p}-\mathbf{p}_0)}; \tag{2}$$

this provides stronger suppression of the Breit-Wigner far from the resonance region.

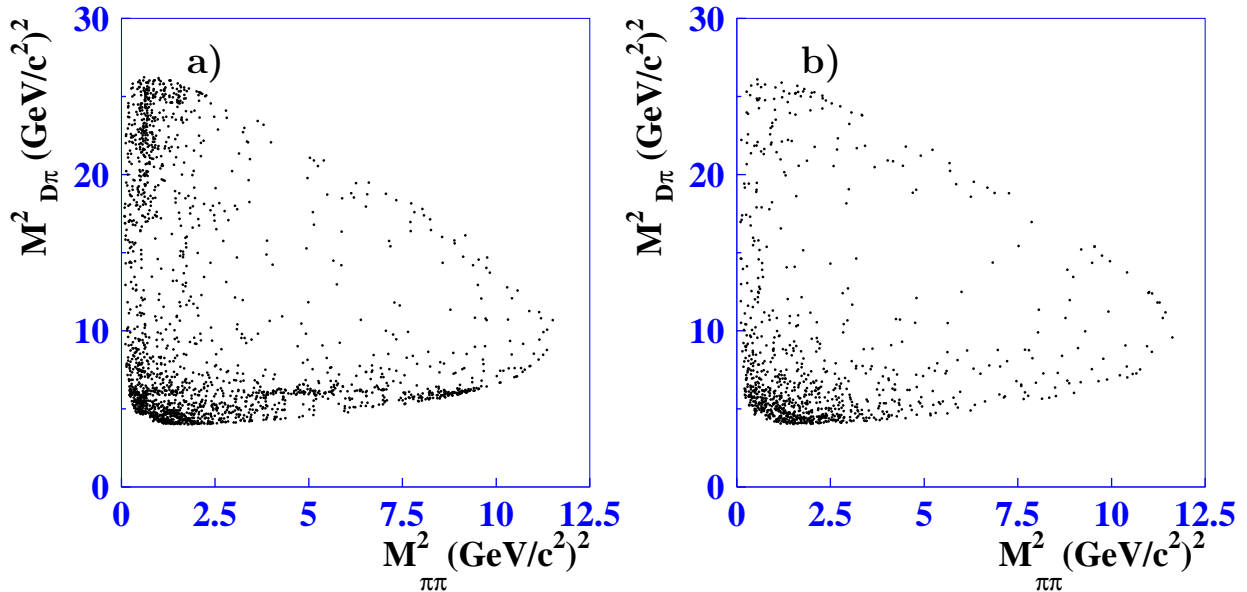


FIG. 5: The Dalitz plot of a) signal events; b) sideband events.

The detector resolution for the invariant mass of the $D\pi(\pi\pi)$ combination is about 2.5 (3.5) MeV which is much smaller than the narrowest peak width 30–40 MeV.

The masses and widths of the $\pi\pi$ resonances (except $f_0(600)$) are fixed at the PDG [1] values. The mass and width of the broad resonance in $(D\pi)$: $M_{D^{*+}} = 2308 \text{ MeV}/c^2$, $\Gamma_{D^{*+}}^0 = 276 \text{ MeV}/c^2$ have been taken from our measurement for the D^{**0} [17].

The masses and widths of the D_2^+ and the f_0 as well as the relative amplitudes and phases are free parameters of the fit. The parameters of the f_0 are quite uncertain and it can also be regarded as a nonresonant S-wave structure.

Table III gives the results of the fit for different models. The contributions of different states are characterized by the branching fractions, which are defined as:

$$Br_i = \frac{a_i^2 \int |A_i(Q)|^2 dQ}{\int |\sum_i a_i e^{i\phi_i} A_i(Q)|^2 dQ}, \quad (3)$$

where $A_i(Q)$ is the corresponding amplitude, a_i and ϕ_i are the amplitude coefficients and phases obtained from the fit. The integration is performed over all the available phase space characterized by the multidimensional vector Q (for decay to 3 spinless particles $dQ \equiv dq^2 dq_1^2$), and i is one of the intermediate states: D_2^* , D_0^* , ρ , f_2 , f_0 , D_v^* , B_v^* or the constant term a_{ps} .

In addition to the main minimum where the likelihood value is maximal \mathcal{L}_0 , there are several local minima with smaller likelihood \mathcal{L} . The value of $(-2 \ln \mathcal{L})$ differs from $(-2 \ln \mathcal{L}_0)$ by 1.9-25. To search for local minima we perform 100 minimizations starting from different points, randomly distributed in the space of the minimized parameters. Local minima appear mainly as a result of different phases between the $D\pi$ and $\pi\pi$ structures. We consider the spread of the branching values as a model error. The central values are the parameters obtained for the main minimum. The spread of the relative phases is rather large. In some

	1	2	3	4	5
	$D_2^*, D_0^*, D_v^*, \rho, f_2, f_0(600)$	$D_2^*, D_0^*, \rho, f_2, f_0(600)$	$D_2^*, D_0^*, D_v^*, \rho, f_2, f_0(600), B_v^*$	$D_2^*, D_0^*, D_v^*, \rho, f_2, f_0(600) + ps$	$D_2^*, D_v^*, \rho, f_2, f_0(600)$
$-2 \ln \mathcal{L}/\mathcal{L}_0$	0	66.9	-9.0	-7.0	37.2
$Br_{D_2^*}(10^{-4})$	3.08 ± 0.22	3.23 ± 0.22	3.19 ± 0.26	3.07 ± 0.22	3.33 ± 0.23
$\phi_{D_0^*}$	-1.82 ± 0.24	-1.52 ± 0.24	-2.15 ± 0.28	-1.81 ± 0.20	–
$Br_{D_0^*}(10^{-4})$	0.60 ± 0.17	0.47 ± 0.15	0.52 ± 0.18	0.62 ± 0.15	–
$\phi_{D_v^*}$	-1.57 ± 0.25	–	-2.18 ± 0.29	-1.54 ± 0.22	-1.90 ± 0.30
$Br_{D_v^*}(10^{-4})$	0.70 ± 0.14	–	0.71 ± 0.14	0.71 ± 0.12	0.62 ± 0.13
ϕ_ρ	1.83 ± 0.24	2.09 ± 0.23	1.23 ± 0.22	2.07 ± 0.24	1.90 ± 0.24
$Br_\rho(10^{-4})$	2.91 ± 0.28	2.82 ± 0.30	2.50 ± 0.33	2.55 ± 0.28	2.97 ± 0.31
ϕ_{f_2}	2.81 ± 0.20	3.05 ± 0.19	2.74 ± 0.19	2.74 ± 0.19	2.89 ± 0.20
$Br_{f_2}(10^{-4})$	1.10 ± 0.19	1.31 ± 0.20	1.18 ± 0.20	1.12 ± 0.17	1.24 ± 0.20
ϕ_{f_0}	0.34 ± 0.18	0.60 ± 0.17	0.34 ± 0.17	0.23 ± 0.17	0.50 ± 0.20
$Br_{f_0}(10^{-4})$	1.75 ± 0.26	1.93 ± 0.31	2.28 ± 0.31	1.81 ± 0.26	1.62 ± 0.28
$\phi_{B_v^*}$	–	–	0.00 ± 0.19	–	–
$Br_{B_v^*}(10^{-4})$	–	–	0.44 ± 0.25	–	–
ϕ_{ps}	–	–	–	1.00 ± 0.21	–
$Br_{ps}(10^{-4})$	–	–	–	0.06 ± 0.05	–
$M_{f_0}, (GeV/c^2)$	0.658 ± 0.062	0.681 ± 0.048	0.649 ± 0.056	0.633 ± 0.052	0.676 ± 0.057
$\Gamma_{f_0}, (GeV/c^2)$	0.94 ± 0.22	0.72 ± 0.14	1.00 ± 0.20	0.88 ± 0.19	0.78 ± 0.17

TABLE III: The fit results for different sets of amplitudes.

cases, the phases “flip” by close to π radians, so that the extraction of relative phases unreliable.

The values of the D_2^{*+} resonance mass and width obtained from the fit are:

$$M_{D_2^{*+}} = (2459.5 \pm 2.3 \pm 0.7_{-0.5}^{+4.9}) \text{MeV}/c^2, \quad \Gamma_{D_2^{*+}} = (48.9 \pm 5.4 \pm 4.2 \pm 1.9) \text{MeV}.$$

These parameters are consistent with the measurements from the FOCUS experiment: $M_{D_2^{*0}} = (2467.6 \pm 1.5 \pm 0.8) \text{MeV}/c^2$, $\Gamma_{D_2^{*0}} = 34.1 \pm 6.5 \pm 4.2 \text{MeV}$ [24].

The product of the branching ratios for D_2^* production obtained in the analysis when the amplitudes are included from above is:

$$\mathcal{B}(\bar{B}^0 \rightarrow D_2^{*+} \pi^-) \times \mathcal{B}(D_2^{*+} \rightarrow D^0 \pi^+) = (3.08 \pm 0.33 \pm 0.09_{-0.02}^{+0.15}) \times 10^{-4},$$

where the indicated errors are the statistical, systematic and model error.

The broad resonance branching fraction assuming 0^+ quantum numbers is:

$$\mathcal{B}(\bar{B}^0 \rightarrow D_0^{*+} \pi^-) \times \mathcal{B}(D_0^{*+} \rightarrow D^0 \pi^+) = (0.60 \pm 0.17 \pm 0.16_{-0.31}^{+0.13}) \times 10^{-4}.$$

The helicity of the $D\pi$ distribution for different regions of q^2 is shown in Fig. 6 together with the efficiency corrected fitting function. The histogram in the region of the D_2^* meson clearly indicates a D-wave. The distributions in the other region show reasonable agreement

of the fitting function and the data but the present statistics does not allow confirmation of the quantum numbers of the resonance. Table II shows that the likelihood changed significantly if we exclude this resonance but differs only slightly if the broad resonance is replaced with a vector or a tensor. We thus set an upper limit for the branching fraction of the scalar $D_0^+ \pi^-$ production:

$$\mathcal{B}(\bar{B}^0 \rightarrow D_0^{*+} \pi^-) \times B(D_0^{*+} \rightarrow D^0 \pi^+) < 1.2 \times 10^{-4} \text{ at } 90\% \text{ C.L..}$$

The uncertainty of the background is one of the main sources of the systematic errors. It is estimated by comparing the fit results for the case when the background shape is taken separately from the lower or upper sideband in the ΔE distribution. The fit is also performed with more restrictive and loose cuts on ΔE , M_{bc} and ΔM_D that changes the signal-to-background ratio by more than a factor of 2. The obtained results are consistent with each other. The maximum difference is taken as an additional estimate of the systematic uncertainty. For the branching fractions, the systematic errors also include uncertainties on track reconstruction and PID efficiency, as well as the error in the $D^0 \rightarrow K^- \pi^+$ absolute branching fraction.

The model uncertainties are estimated by comparing fit results for the case of different models and for the values of the parameter r of the transition form factor that range from 0 to 3 $(\text{GeV}/c)^{-1}$.

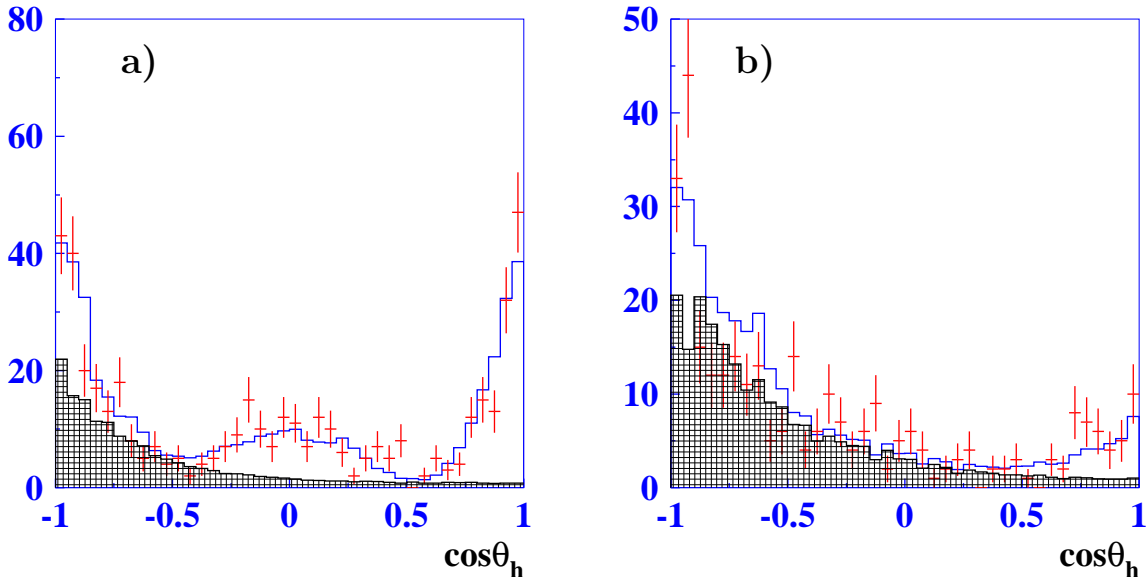


FIG. 6: Helicity of the $D\pi$ distribution for experimental events (points) and for MC simulation (histogram). The hatched distribution shows the background from the ΔE sideband region with a proper normalization. (a) corresponds to the D_2 region $|M_{D\pi} - 2.46| < 0.1 \text{ GeV}/c^2$; (b) - D_0 region $|M_{D\pi} - 2.30| < 0.1 \text{ GeV}/c^2$.

The helicities of the $\pi\pi$ system in the $M_{\pi\pi}$ range of ρ , f_2 and below the ρ where the broad resonance dominates are shown in Fig. 7. For the positive helicity range where the $D\pi$ contribution is suppressed, a clear P -wave structure for ρ and D -wave for f_2 is observed. The

branching ratios for the $f_0(600)$ is $\mathcal{B}(\bar{B}^0 \rightarrow f_0 D^0) \mathcal{B}(f_0 \rightarrow \pi^+ \pi^-) = (1.75 \pm 0.26 \pm 0.35_{-0.18}^{+0.55}) \times 10^{-4}$. This process can also have a contribution from some nonresonance background. The branching ratios for the ρ and the f_2 are as follows:

$$\mathcal{B}(\bar{B}^0 \rightarrow f_2 D^0) \mathcal{B}(f_2 \rightarrow \pi^+ \pi^-) = (1.10 \pm 0.19 \pm 0.21_{-0.01}^{+0.18}) \times 10^{-4}.$$

Taking into account the PDG value of the branching fraction $\mathcal{B}(f_2 \rightarrow \pi\pi) = 0.848_{-0.013}^{+0.025}$ and Clebsch-Gordan coefficients, we obtain:

$$\mathcal{B}(\bar{B}^0 \rightarrow f_2 D^0) = (1.95 \pm 0.34 \pm 0.38_{-0.02}^{+0.32}) \times 10^{-4},$$

$$\mathcal{B}(\bar{B}^0 \rightarrow \rho^0 D^0) = (2.91 \pm 0.28 \pm 0.33_{-0.54}^{+0.08}) \times 10^{-4}.$$

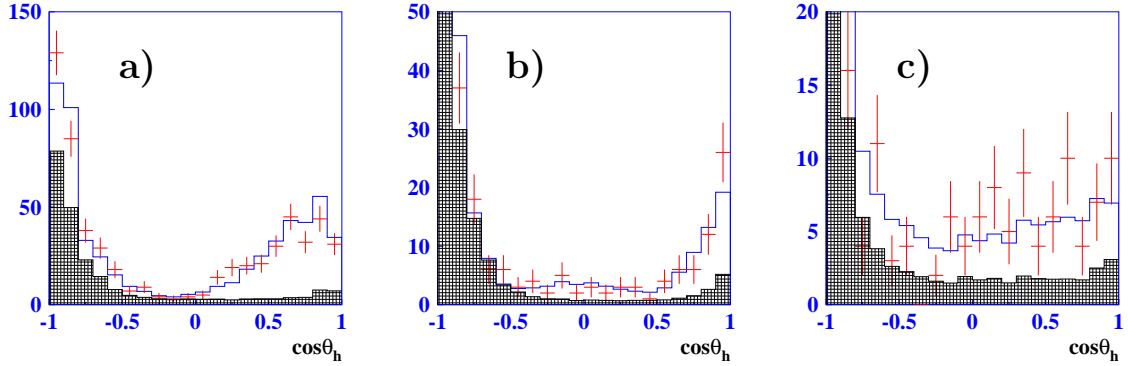


FIG. 7: Helicity distribution for experimental events (points) and for MC simulation (histogram). The hatched distribution shows the background distribution from the ΔE sideband region with a proper normalization. (a) corresponds to the ρ region $|M_{\pi\pi} - 0.78| < 0.2 \text{ GeV}/c^2$; (b) – f_2 region $|M_{\pi\pi} - 1.20| < 0.1 \text{ GeV}/c^2$; (c) – f_0 region $M_{\pi\pi} < 0.60 \text{ GeV}/c^2$.

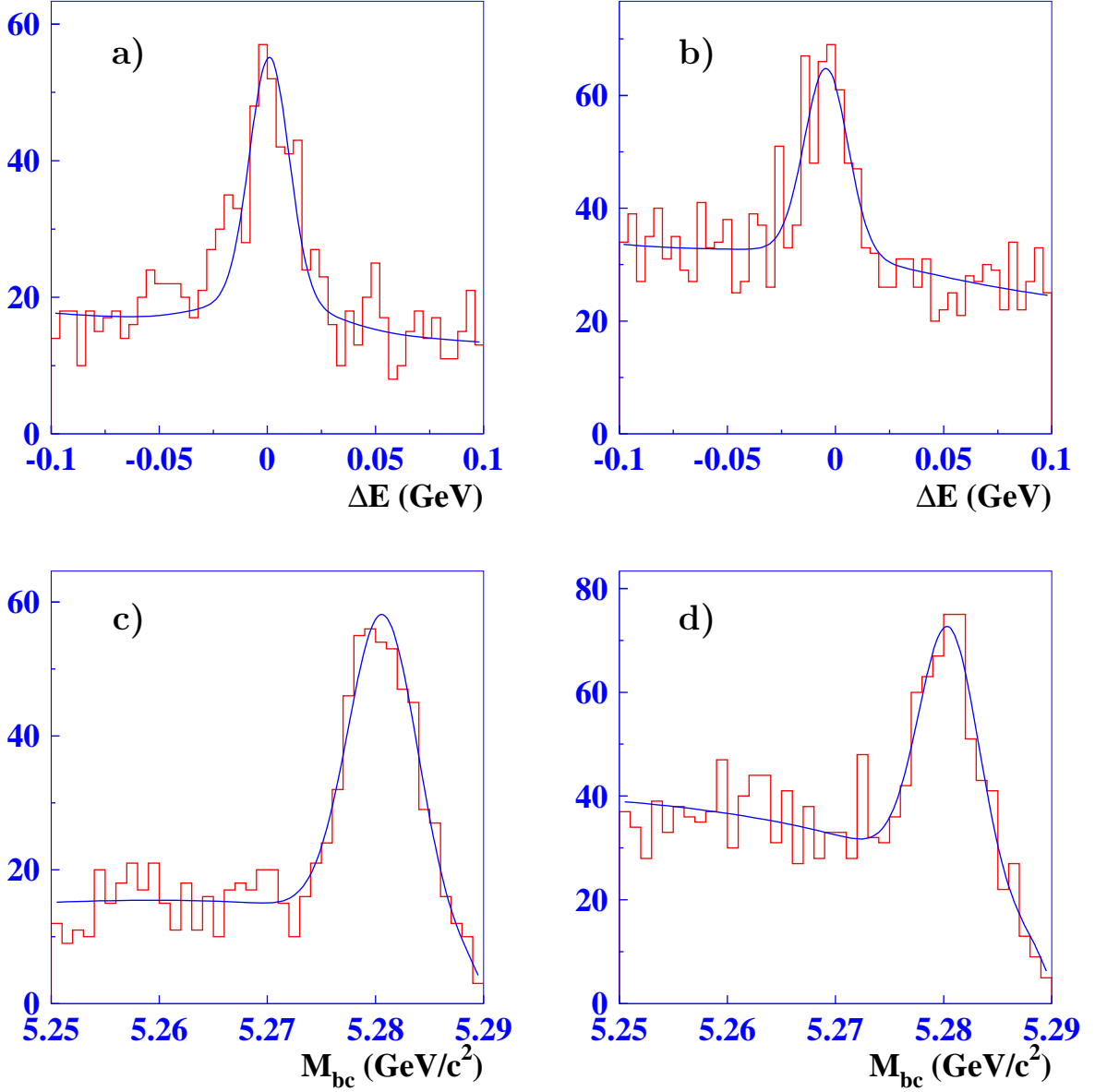
$\bar{B}^0 \rightarrow D^{*0} \pi^+ \pi^-$ ANALYSIS.

For D^* reconstruction, the $D^{*0} \rightarrow D^0 \pi^0$ decay is used with two decay modes of the D^0 : $D^0 \rightarrow K^- \pi^+$ and $D^0 \rightarrow K^- \pi^+ \pi^+ \pi^-$. The event distributions in ΔE and M_{bc} are shown in Fig. 8. In each mode the number of signal events is obtained in a way similar to that described for the $D\pi\pi$ selection. The observed signal yields of $N_{K\pi} = 278 \pm 23$ and $N_{K3\pi} = 269 \pm 29$ for the $K\pi$ and $K\pi\pi\pi$ modes, respectively, are consistent when efficiencies determined from MC, and the following D branching fractions are used: $(3.80 \pm 0.09)\%$ for $K^- \pi^+$ and $(7.46 \pm 0.31)\%$ for $K^- \pi^+ \pi^+ \pi^-$. The branching fraction of $(D^* \rightarrow D\pi)\pi\pi$ events, calculated from the weighted average of the values obtained for the two modes, is:

$$\mathcal{B}(\bar{B}^0 \rightarrow D^{*0} \pi^+ \pi^-) = (1.09 \pm 0.08 \pm 0.16) \times 10^{-3},$$

where the first error is statistical and the second is systematic. This measurement is about 2.5σ larger than the previous result [22] of $(0.62 \pm 0.22 \pm 0.22) \times 10^{-3}$. We consider the previous measurement to be a statistical fluctuation. The systematic error contributions are listed in Table IV.

The background shape uncertainty and the effect of cut boundaries were estimated in the same way as for the $D\pi\pi$ analysis.



$D \rightarrow K\pi$

$D \rightarrow K3\pi$

FIG. 8: Distribution of $\bar{B}^0 \rightarrow D^{*0}\pi^+\pi^-$ events in ΔE and M_{bc} plots with D reconstruction in $K\pi$ mode – (a), (c) and in $K3\pi$ mode – (b), (d). (a), (b) ΔE distributions. (c), (d) M_{bc} distributions.

$B \rightarrow D^*\pi\pi$ coherent amplitude analysis

In this final state we have a decaying vector D^* particle. There are two additional degrees of freedom and, in addition to the $D^*\pi$ and $\pi\pi$ invariant masses squared (q^2, q_1^2), two other variables are needed to specify the final state. The variables are chosen to be the angle α between the pions from the D^{**} and D^* decay in the D^* rest frame, and the azimuthal angle γ of the pion from the D^* relative to the $B \rightarrow D^*\pi\pi$ decay plane. For the case of the $\pi\pi$

Source	$\sigma_{sys}, \%$
$Br(D^{*0}, D^0)$	5.3
Tracking	4.3
π^0	6
PID	5
MC	3
Background	10
Total	14.7

TABLE IV: Contributions to the systematic error for $B \rightarrow D^* \pi \pi$.

structure analysis another set of parameters can be chosen: $\pi\pi$ square mass (q_1^2); the helicity angle θ' of the $\pi\pi$ -meson — the angle between the positive pion from this meson decay and the D^* direction in the $\pi\pi$ meson rest frame; the helicity angle α' of the D^* meson — the angle between the pion from the D^* decay and the $\pi\pi$ -meson in the D^* rest frame; and the angle γ' between the decay planes of the D^* and the $\pi\pi$ -meson.

For further analysis, events satisfying the selection criteria described in the first section within the signal region $((\Delta E + \kappa(M_{bc} - M_B))/\sigma_{\Delta E})^2 + ((M_{bc} - M_B)/\sigma_{M_{bc}})^2 < s$ are selected. The parameters $\sigma_{\Delta E} = 11 \text{ MeV}/c^2$, $\sigma_{M_{bc}} = 2.7 \text{ MeV}/c^2$, $\kappa = 0.9$ are obtained from a fit to experimental data, and the coefficient κ takes into account the correlation between M_{bc} and ΔE . The parameter s is selected to be 4 for the mode with $D \rightarrow K\pi$ and 3 for $D \rightarrow K\pi\pi\pi$ to have a similar signal-to-background ratio. To understand the contribution and shape of the background, we use events in the sidebands $((\Delta E \pm 65 \text{ MeV} + \kappa(M_{bc} - M_B))/\sigma_{\Delta E})^2 + ((M_{bc} - M_B)/\sigma_{M_{bc}})^2 < s$.

The $D^*\pi$ and $\pi\pi$ mass distributions for the signal and sideband events are shown in Fig. 9 and 10. There is a clear peak of the narrow states D_2^{*+} and D_1^+ with a negligible contribution of the broad states in the $D\pi$ distribution. In the $\pi\pi$ distribution the peaks of ρ and $f_2(1270)$ are clearly seen while the peak-like structure around $2.6 \text{ GeV}/c^2$ is the reflection of the $D\pi$ angular distribution. In order to have the same Dalitz plot boundary for events from both the signal and the sideband regions as well as to decrease the smearing effect introduced by the detector resolution, mass-constrained fits of $D\pi$ to $M_{D^{*+}}$ and $D^*\pi\pi$ to M_B are performed.

To extract the amplitudes and phases for different intermediate states, an unbinned likelihood fit in the four-dimensional phase space is performed. Assuming that the background distribution $\mathcal{B}(q^2, q_1^2, \alpha, \gamma)$ in the signal region has the same shape as in the ΔE sideband, we obtain the $\mathcal{B}(q^2, q_1^2, \alpha, \gamma)$ dependence from a fit of the sideband distribution to a smooth four-dimensional function.

The number of background events in the signal region is normalized according to the relative areas of the signal and the sideband regions. The signal is parameterized as a sum of the amplitudes of an intermediate tensor (D_2^*), two axial vector mesons (D_1', D_1), and three resonances ρ , f_2 and $f_0(600)$ in the $\pi\pi$ mode. For ρ and f_2 there can be three different amplitudes depending on the relative polarizations of the decay products: A_0 , A_\perp and A_\parallel .

Finally, the signal is expressed as follows:

$$S(q^2, q_1^2, \alpha, \gamma) = |a_2 A^{(2)}(q^2, q_1^2, \alpha, \gamma) + a_1 e^{i\phi_1} A^{(n)}(q^2, q_1^2, \alpha, \gamma) + a_w e^{i\phi_w} A^{(w)}(q^2, q_1^2, \alpha, \gamma)$$

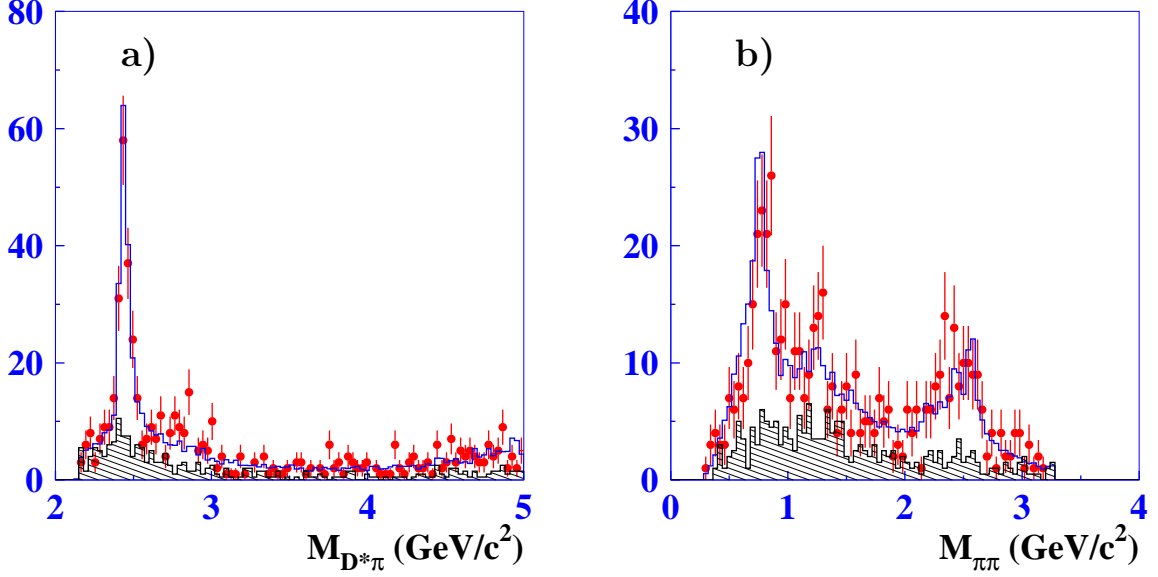


FIG. 9: Mass distribution of $D^*\pi$ and $\pi\pi$ events. Points are the experimental data, the hatched histogram is the background distribution obtained from the sidebands, the open histogram is MC simulation with the amplitudes and parameters of the intermediate resonances obtained from the fit.

$$\begin{aligned}
& +a_\rho e^{i\phi_\rho} ((1 - a_\parallel^\rho - a_\perp^\rho) A_0^{(\rho)}(q^2, q_1^2, \alpha, \gamma) + a_\parallel^\rho e^{i\phi_\parallel^\rho} A_\parallel^{(\rho)}(q^2, q_1^2, \alpha, \gamma) \\
& + a_\perp^\rho e^{i\phi_\perp^\rho} A_\perp^{(\rho)}(q^2, q_1^2, \alpha, \gamma)) \\
& + a_{f_2} e^{i\phi_{f_2}} ((1 - a_\parallel^{f_2} - a_\perp^{f_2}) A_0^{(f_2)}(q^2, q_1^2, \alpha, \gamma) + a_\parallel^{f_2} e^{i\phi_\parallel^{f_2}} A_\parallel^{(f_2)}(q^2, q_1^2, \alpha, \gamma) \\
& + a_\perp^{f_2} e^{i\phi_\perp^{f_2}} A_\perp^{(f_2)}(q^2, q_1^2, \alpha, \gamma)) \\
& + a_{f_0} A^{(f_0)}(q^2, q_1^2, \alpha, \gamma) + a_{ps}|^2.
\end{aligned} \tag{4}$$

The MC gives the resolution in invariant mass of about $1.9 \text{ MeV}/c^2$, which is smaller than the resonance widths and can be neglected.

Each resonance is described by a relativistic Breit-Wigner function with a width depending on q^2 . The angular dependence for each resonance corresponds to the spins of the intermediate and final state particles [17]. The amplitudes of $B \rightarrow D^*\rho$ and $B \rightarrow D^*f_2$ decays have the following angular distributions:

$$\begin{aligned}
A_0^\rho & \sim \cos \alpha' \cos \theta' \\
A_\parallel^\rho & \sim \sin \alpha' \sin \theta' \cos \gamma' \\
A_\perp^\rho & \sim \sin \alpha' \sin \theta' \sin \gamma'
\end{aligned} \tag{5}$$

$$\begin{aligned}
A_0^{f_2} & \sim \cos \alpha' (\cos^2 \theta' - 1/3) \\
A_\parallel^{f_2} & \sim \sin \alpha' \sin \theta' \cos \theta' \cos \gamma' \\
A_\perp^{f_2} & \sim \sin \alpha' \sin \theta' \cos \theta' \sin \gamma'
\end{aligned} \tag{6}$$

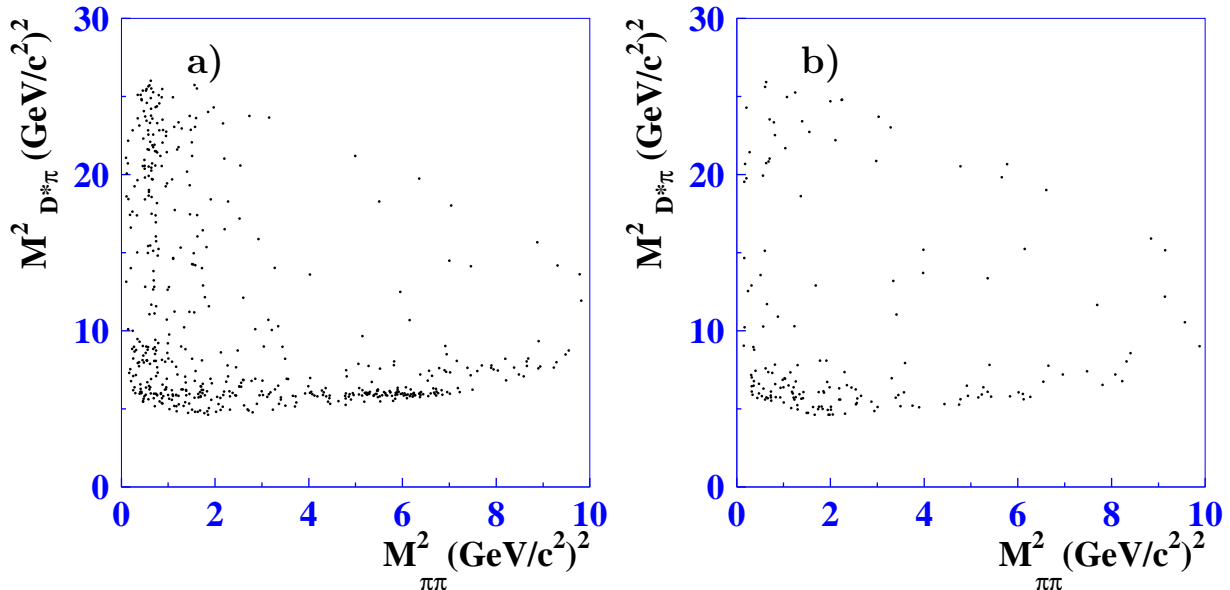


FIG. 10: The Dalitz plot of (a) signal events; (b) sideband events.

	$D_2^*, D_1, D_1', \rho, f_0(600)$		
	f_2	$f_0(1370)$	no
$-2 \ln \mathcal{L}/\mathcal{L}_0$	0	11	41

TABLE V: Comparison of the models with different resonances included in the fits.

Table VI shows the results of the fit for different models. If we remove the D_1' meson from Eq. 4, the likelihood does not change significantly. If we remove the f_2 instead, the likelihood increases by 41. Adding the phase space term does not improve the likelihood significantly. Replacing the f_2 meson with an $f_0(1370)$ results in a worse likelihood value as shown in Table V.

The masses and widths of the $\pi\pi$ resonances are fixed at their PDG values; $M_{D_2^{*+}}$, and $\Gamma_{D_2^{*+}}^0$ are taken from the $D\pi\pi$ fit; and $M_{D_1} = 2427 \text{ MeV}/c^2$, $\Gamma_{D_1}^0 = 384 \text{ MeV}/c^2$ have been taken from our measurement for D^{**0} [17]. The mass $M_{D_1^+}$ and width $\Gamma_{D_1^+}$ as well as the branching fractions and phases of the amplitudes were free parameters of the fit.

In addition to the main minimum, there are several local minima that differ in $-2 \ln \mathcal{L}/\mathcal{L}_0$ by 2.1 to 25. The main minimum and local minima are treated in the same way as for $D\pi\pi$.

Figs. 9 and 11 demonstrate the comparison of data and the MC simulation generated according to Eq. (4) with parameters obtained from the fit. The distributions of the helicities of D^{**} and D^* and the angle γ in different q^2 regions demonstrate reasonable agreement of the experimental data and fit result.

For the D_1 meson we obtain the following parameters:

$$M_{D_1^+} = (2428.2 \pm 2.9 \pm 1.6 \pm 0.6) \text{ MeV}/c^2, \quad \Gamma_{D_1^+} = (34.9 \pm 6.6_{-0.9}^{+4.1} \pm 4.1) \text{ MeV}.$$

These parameters are in good agreement with the CLEO measurement for D_1^0 : $M_{D_1^0} = (2425 \pm 2 \pm 2) \text{ MeV}/c^2$, $\Gamma_{D_1^0} = (26_{-7}^{+8} \pm 4) \text{ MeV}$ [9].

	D_2^*, D_1, D_1'	D_2^*, D_1	D_2^*, D_1, D_1'	D_2^*, D_1, D_1'
	$\rho, f_2, f_0(600)$	$\rho, f_2, f_0(600)$	$\rho, f_0(600)$	$\rho, f_2, f_0(600) + ps$
$-2 \ln \mathcal{L}/\mathcal{L}_0$	0	-4	+41	-1
$Br_{D_2^*}(10^{-4})$	2.45 ± 0.42	2.45 ± 0.42	2.48 ± 0.43	2.43 ± 0.41
ϕ_{D_1}	0.908 ± 0.145	0.907 ± 0.145	0.837 ± 0.139	0.766 ± 0.147
$Br_{D_1}(10^{-4})$	3.68 ± 0.60	3.71 ± 0.62	4.03 ± 0.84	3.63 ± 0.61
$\phi_{D_1'}$	-0.197 ± 0.584	–	-0.316 ± 0.670	-0.121 ± 0.556
$Br_{D_1'}(10^{-4})$	0.14 ± 0.13	–	0.11 ± 0.12	0.14 ± 0.14
ϕ_{ps}	–	–	–	2.594 ± 0.551
$Br_{ps}(10^{-4})$	–	–	–	0.00 ± 0.17
ϕ_ρ	2.566 ± 0.333	2.543 ± 0.337	2.032 ± 0.326	2.560 ± 0.327
$Br_\rho(10^{-4})$	3.73 ± 0.87	3.78 ± 0.87	3.89 ± 0.96	3.74 ± 0.85
ϕ_{f_2}	0.440 ± 0.413	0.411 ± 0.425	–	0.429 ± 0.453
$Br_{f_2}(10^{-4})$	1.05 ± 0.37	1.05 ± 0.37	–	0.98 ± 0.35
ϕ_{f_0}	-2.263 ± 0.646	-2.190 ± 0.643	-2.823 ± 0.498	-2.181 ± 0.597
$Br_{f_0}(10^{-4})$	0.17 ± 0.11	0.16 ± 0.11	0.32 ± 0.17	0.17 ± 0.11
$a_{ }^\rho$	0.204 ± 0.059	0.198 ± 0.058	0.176 ± 0.061	0.211 ± 0.059
a_\perp^ρ	0.067 ± 0.038	0.065 ± 0.038	0.105 ± 0.042	0.066 ± 0.038
ϕ_\perp^ρ	0.678 ± 0.348	0.686 ± 0.351	0.693 ± 0.307	0.624 ± 0.358
a_0^ρ	0.730 ± 0.058	0.737 ± 0.057	0.719 ± 0.059	0.723 ± 0.058
ϕ_{ρ_2}	2.046 ± 0.229	2.031 ± 0.229	2.269 ± 0.250	2.030 ± 0.225
$a_0^{f_2}$	0.623 ± 0.137	0.616 ± 0.143	–	0.646 ± 0.142
$a_\perp^{f_2}$	0.080 ± 0.084	0.092 ± 0.091	–	0.082 ± 0.085
$\phi_\perp^{f_2}$	-3.036 ± 0.687	-2.983 ± 0.672	–	-3.129 ± 0.752
$a_{ }^{f_2}$	0.297 ± 0.137	0.292 ± 0.142	–	0.273 ± 0.143
$\phi_{ }^{f_2}$	-0.895 ± 0.489	-0.846 ± 0.506	–	-0.926 ± 0.551

TABLE VI: The fit results for different sets of amplitudes.

The preliminary results for the product of the branching ratios of the D^{**} 's are the following:

$$\begin{aligned} \mathcal{B}(\bar{B}^0 \rightarrow D_1^+ \pi^-) \times B(D_1^+ \rightarrow D^{*0} \pi^+) &= (3.68 \pm 0.60_{-0.40}^{+0.71+0.65}) \times 10^{-4}, \\ \mathcal{B}(\bar{B}^0 \rightarrow D_2^{*+} \pi^-) \times B(D_2^{*+} \rightarrow D^{*0} \pi^+) &= (2.45 \pm 0.42_{-0.45}^{+0.35+0.39}) \times 10^{-4}, \\ \mathcal{B}(\bar{B}^0 \rightarrow D_1'^+ \pi^-) \times B(D_1'^+ \rightarrow D^{*0} \pi^+) &= (0.14 \pm 0.13 \pm 0.12_{-0.10}^{+0.00}) \times 10^{-4}. \end{aligned}$$

The last value is not statistically significant and corresponds to an upper limit:

$$\mathcal{B}(\bar{B}^0 \rightarrow D_1'^+ \pi^-) \times B(D_1'^+ \rightarrow D^{*0} \pi^+) < 0.7 \times 10^{-4} \text{ at } 90\% \text{ C.L.}$$

Including a contact term improves the likelihood but without high significance (see Table VI).

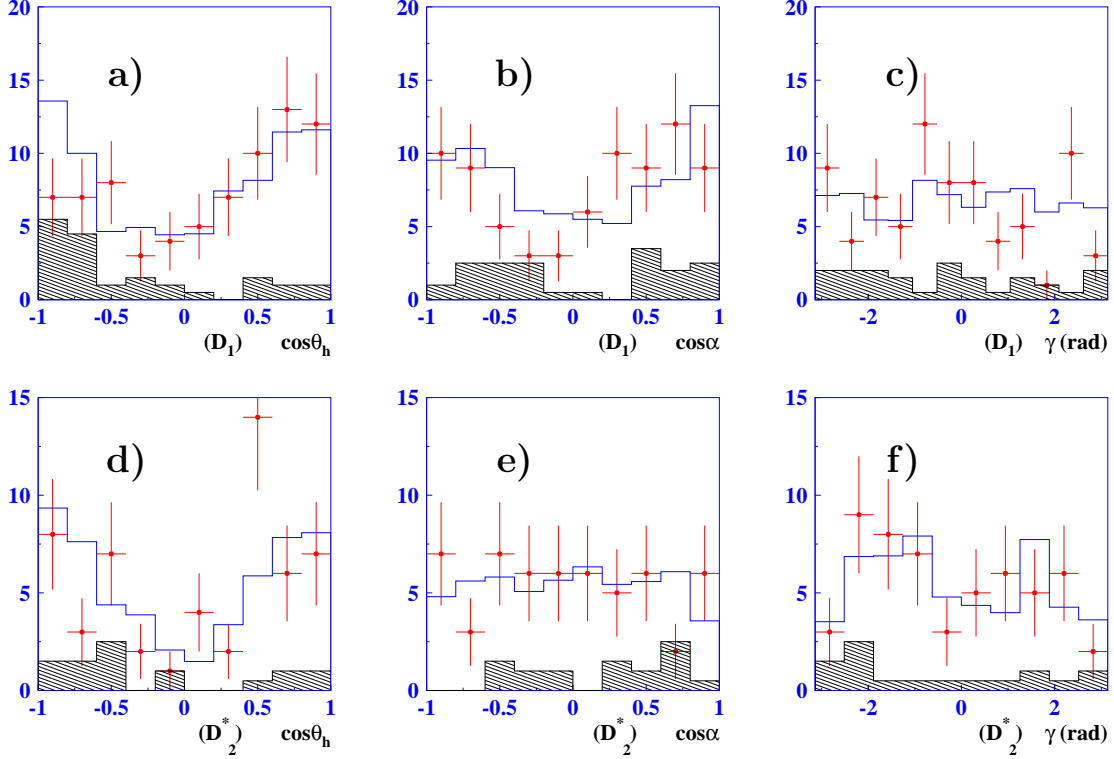


FIG. 11: The distribution of the data for the D_1 region: (a)-(c) $|M_{D^*\pi} - 2.41| < 0.03 \text{ GeV}/c^2$ and the D_2^* region: $|M_{D^*\pi} - 2.45| < 0.025 \text{ GeV}/c^2$ (d)-(f). (a), (d) $\cos\theta$ – helicity angle of D^{**} ; (b), (e) $\cos\alpha$ – helicity angle of D^* ; (c), (f) azimuthal angle γ . The points are experimental data, the histogram is MC with fitted parameters, and the hatched histogram is the background contribution (from sideband).

The helicity of the $\pi\pi$ system and the D^* as well as the azimuthal angle γ' are plotted in Fig. 12 for the $M_{\pi\pi}$ range of the ρ and the f_2 .

The branching ratio for the $f_0(600)$ production is comparable with zero: $\mathcal{B}(\bar{B}^0 \rightarrow f_0 D^0) \mathcal{B}(f_0 \rightarrow \pi^+\pi^-) = (0.17 \pm 0.11 \pm 0.10_{-0.05}^{+0.18}) \times 10^{-4}$. This contribution can also be regarded as some nonresonance background.

The branching ratios observed for the ρ and the f_2 are as follows:

$$\mathcal{B}(\bar{B}^0 \rightarrow \rho^0 D^{*0}) = (3.73 \pm 0.87 \pm 0.46_{-0.08}^{+0.18}) \times 10^{-4},$$

$$\mathcal{B}(\bar{B}^0 \rightarrow f_2 D^{*0}) \mathcal{B}(f_2 \rightarrow \pi^+\pi^-) = (1.05 \pm 0.37 \pm 0.34_{-0.33}^{+0.45}) \times 10^{-4}.$$

Taking into account the branching fraction of $\mathcal{B}(f_2 \rightarrow \pi^+\pi^-)$ we obtain:

$$\mathcal{B}(\bar{B}^0 \rightarrow f_2 D^{*0}) = (1.86 \pm 0.65 \pm 0.60_{-0.52}^{+0.80}) \times 10^{-4}.$$

In spite of the limited statistics, we can determine the contribution of different polarization amplitudes for ρ and f_2 :

$$a_0^\rho = 0.73 \pm 0.06 \pm 0.10 \pm 0.09$$

$$a_{||}^\rho = 0.20 \pm 0.06 \pm 0.03 \pm 0.10$$

$$a_{\perp}^{\rho} = 0.07 \pm 0.04 \pm 0.05_{-0.03}^{+0.19}$$

$$a_0^{f_2} = 0.62 \pm 0.14 \pm 0.25 \pm 0.24$$

$$a_{\parallel}^{f_2} = 0.30 \pm 0.14_{-0.27-0.27}^{+0.07+0.09}$$

$$a_{\perp}^{f_2} = 0.08 \pm 0.08_{-0.03-0.02}^{+0.21+0.21}$$

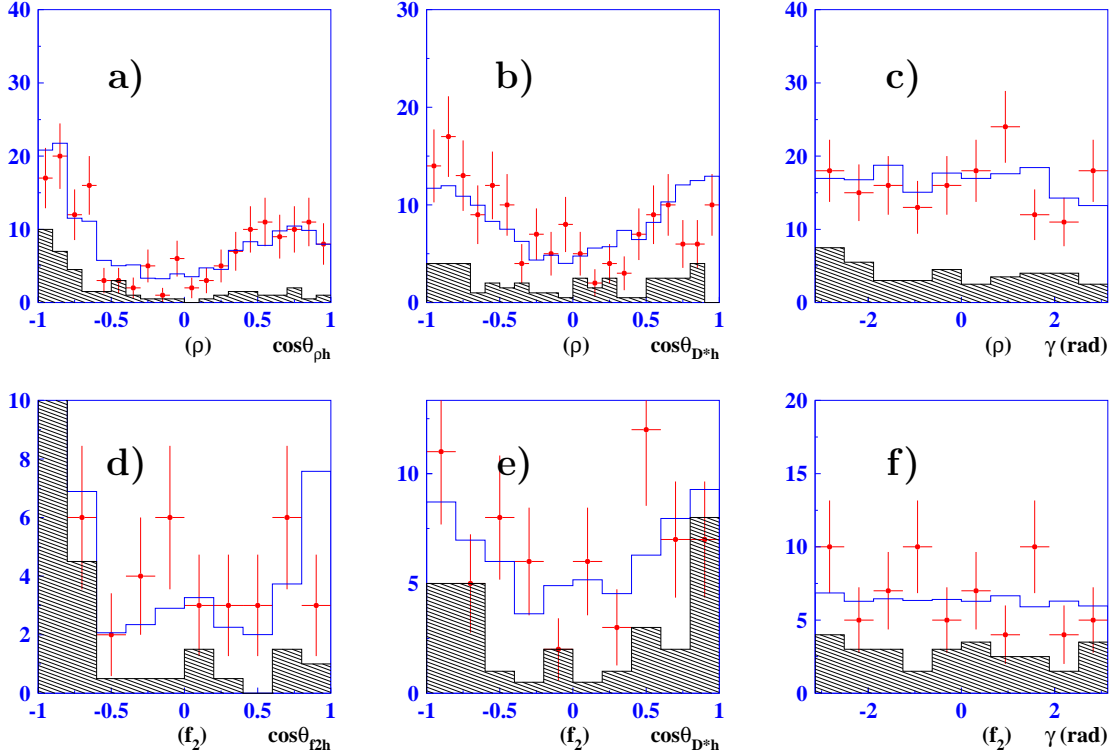


FIG. 12: Helicity distribution for the ρ region: (a)-(c) $|M_{\pi\pi} - .80| < 0.20 \text{ GeV}/c^2$ and the D_2^* region: $|M_{\pi\pi} - 1.225| < 0.125 \text{ GeV}/c^2$ (d)-(f). (a), (d) $\cos\theta$ – helicity angle of D^{**} ; (b), (e) $\cos\alpha$ – helicity angle of D^* ; (c), (f) azimuthal angle γ . experimental events (points) and for fast MC simulation (histogram). The hatched distribution shows the background distribution from the ΔE sideband region with a proper normalization.

Results and discussion

The branching-fraction products obtained for the narrow ($j = 3/2$) resonances are similar to those obtained in the case of charged B decays as shown in Table VII. The measured values of the branching fractions of the broad resonance D_0^{*+} and D_1^{*+} production in neutral B decay are, however, significantly lower than those for charged B decays. One possible explanation for this phenomenon is that for charged B decay to $D^{**}\pi$, the amplitude receives contributions from both tree and the color suppressed diagrams as shown in Fig. 13. Production of D^{**} via tree-diagrams is described by the Isgur-Wise functions $\tau_{1/2}$ and $\tau_{3/2}$. According to the sum rule [25, 26], $\tau_{1/2} \ll \tau_{3/2}$ and one would expect the suppression of the

	Neutral B	Charged B [17]
$\mathcal{B}(\bar{B} \rightarrow D_2^* \pi^-) \mathcal{B}(D_2^* \rightarrow D^* \pi)$	$(2.45 \pm 0.42^{+0.35+0.39}_{-0.45-0.17}) \times 10^{-4}$	$(1.8 \pm 0.3 \pm 0.3 \pm 0.2) \times 10^{-4}$
$\mathcal{B}(\bar{B} \rightarrow D_1 \pi^-) \mathcal{B}(D_1 \rightarrow D^* \pi)$	$(3.68 \pm 0.60^{+0.71+0.65}_{-0.40-0.30}) \times 10^{-4}$	$(6.8 \pm 0.7 \pm 1.3 \pm 0.3) \times 10^{-4}$
$\mathcal{B}(\bar{B} \rightarrow D_2^* \pi^-) \mathcal{B}(D_2^* \rightarrow D \pi)$	$(3.08 \pm 0.33 \pm 0.09^{+0.15}_{-0.02}) \times 10^{-4}$	$(3.4 \pm 0.3 \pm 0.6 \pm 0.4) \times 10^{-4}$
$\mathcal{B}(\bar{B} \rightarrow D_1' \pi^-) \mathcal{B}(D_1' \rightarrow D^* \pi)$	$< 0.7 \times 10^{-4}$ at 90 % C.L.	$(5.0 \pm 0.4 \pm 1.0 \pm 0.4) \times 10^{-4}$
$\mathcal{B}(\bar{B} \rightarrow D_0^* \pi) \mathcal{B}(D_0^* \rightarrow D \pi)$	$< 1.2 \times 10^{-4}$ at 90 % C.L.	$(6.1 \pm 0.6 \pm 0.9 \pm 1.6) \times 10^{-4}$

TABLE VII: Comparison of branching-fraction products for neutral and charged B decays.

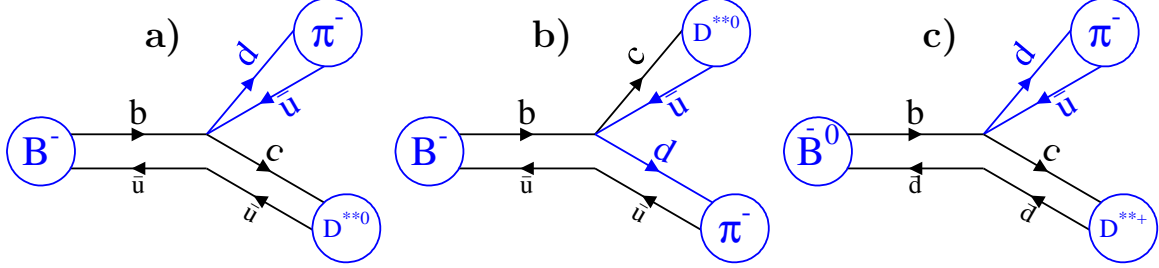


FIG. 13: Feynman diagrams for charged (a),(b) and neutral (c) B decays.

broad state production. For the color suppressed diagrams, however, D^{**} 's are produced by another mechanism and the amplitudes are characterized by the constants $f_{D(3/2)}$ and $f_{D(1/2)}$ and $f_{D(3/2)} \ll f_{D(1/2)}$. The production of the broad resonances D_0^{*0} and $D_1^{\prime 0}$ in charged B decay is probably amplified by the color suppressed amplitude.

CONCLUSION

A study of neutral B to $D^0 \pi^+ \pi^-$ and $D^{*0} \pi^+ \pi^-$ decays has been presented. We have measured the total branching fractions of the three-body decays: $\mathcal{B}(\bar{B}^0 \rightarrow D^0 \pi^+ \pi^-) = (1.07 \pm 0.06 \pm 0.10) \times 10^{-3}$ and $\mathcal{B}(\bar{B}^0 \rightarrow D^{*0} \pi^+ \pi^-) = (1.09 \pm 0.08 \pm 0.16) \times 10^{-3}$ and the two-body decay: $\mathcal{B}(\bar{B}^0 \rightarrow D^{*+} \pi^-) = (2.30 \pm 0.06 \pm 0.19) \times 10^{-3}$.

The dynamics of these three-body decays has been studied. The $D^0 \pi^+ \pi^-$ final state is described by the production of $D_2^* \pi^-$ with subsequent decays of $D_2^* \rightarrow D \pi$ and $D \rho$, $D f_2$ and a broad scalar ($\pi \pi$) structure. From a Dalitz distribution analysis we have obtained the branching fraction product for D_2^{*+} :

$$\mathcal{B}(\bar{B}^0 \rightarrow D_2^{*+} \pi^-) \times \mathcal{B}(D_2^{*+} \rightarrow D^0 \pi^+) = (3.08 \pm 0.33 \pm 0.09^{+0.15}_{-0.02}) \times 10^{-4}.$$

The values obtained for the mass and width of the tensor meson D_2^{*+} are:

$$M_{D_2^{*+}} = (2459.5 \pm 2.3 \pm 0.7^{+4.9}_{-0.5}) \text{MeV}/c^2, \quad \Gamma_{D_2^{*+}} = (48.9 \pm 5.4 \pm 4.2 \pm 1.9) \text{MeV}.$$

The upper limit for the contribution of the scalar D_0^{*+} meson assuming its mass and width of D_0^0 is:

$$\mathcal{B}(\bar{B}^0 \rightarrow D_0^{*+} \pi^-) \times \mathcal{B}(D_0^{*+} \rightarrow D^0 \pi^+) < 1.2 \times 10^{-4} \text{ at 90 \% C.L..}$$

The branching fractions for $D\rho$ and Df_2 productions have been measured:

$$\mathcal{B}(\bar{B}^0 \rightarrow \rho^0 D^0) = (2.91 \pm 0.28 \pm 0.33_{-0.54}^{+0.08}) \times 10^{-4}$$

$$\mathcal{B}(\bar{B}^0 \rightarrow f_2 D^0) = (1.95 \pm 0.34 \pm 0.38_{-0.02}^{+0.32}) \times 10^{-4}.$$

The last result represents a first observation.

The $D^*\pi\pi$ final state is described by the production of $D_2^*\pi$ and $D_1\pi$ with subsequent decays of $D^{**} \rightarrow D^*\pi$ and $D^*\rho$, D^*f_2 . From a phase space analysis, we obtain the branching fractions product for D^{**0} :

$$\mathcal{B}(\bar{B}^0 \rightarrow D_1^+\pi^-) \times B(D_1^+ \rightarrow D^{*0}\pi^+) = (3.68 \pm 0.60_{-0.40-0.30}^{+0.71+0.65}) \times 10^{-4},$$

$$\mathcal{B}(\bar{B}^0 \rightarrow D_2^{*+}\pi^-) \times B(D_2^{*+} \rightarrow D^{*0}\pi^+) = (2.45 \pm 0.42_{-0.45-0.17}^{+0.35+0.39}) \times 10^{-4}$$

and set an upper limit on the production of the broad D_1' resonance:

$$\mathcal{B}(\bar{B}^0 \rightarrow D_1'^+\pi^-) \times B(D_1'^+ \rightarrow D^{*0}\pi^+) < 0.7 \times 10^{-4} \text{ at } 90\% \text{ C.L..}$$

For the D_1 meson mass and width we obtain the following values:

$$M_{D_1^+} = (2428.2 \pm 2.9 \pm 1.6 \pm 0.6) \text{ MeV}/c^2, \quad \Gamma_{D_1^+} = (34.9 \pm 6.6_{-0.9}^{+4.1} \pm 4.1) \text{ MeV}.$$

The branching fraction of $D^*\rho$ and D^*f_2 has been measured:

$$\mathcal{B}(\bar{B}^0 \rightarrow \rho^0 D^{*0}) = (3.73 \pm 0.87 \pm 0.46_{-0.08}^{+0.18}) \times 10^{-4}$$

$$\mathcal{B}(\bar{B}^0 \rightarrow f_2 D^{*0}) = (1.86 \pm 0.65 \pm 0.60_{-0.52}^{+0.80}) \times 10^{-4},$$

These are the first measurements of these processes. We also observe dominance of the longitudinal polarization amplitude for $B \rightarrow D^*\rho$ and $B \rightarrow D^*f_2$.

All results are preliminary.

Acknowledgments

We thank the KEKB group for the excellent operation of the accelerator, the KEK Cryogenics group for the efficient operation of the solenoid, and the KEK computer group and the National Institute of Informatics for valuable computing and Super-SINET network support. We acknowledge support from the Ministry of Education, Culture, Sports, Science, and Technology of Japan and the Japan Society for the Promotion of Science; the Australian Research Council and the Australian Department of Education, Science and Training; the National Science Foundation of China under contract No. 10175071; the Department of Science and Technology of India; the BK21 program of the Ministry of Education of Korea and the CHEP SRC program of the Korea Science and Engineering Foundation; the Polish State Committee for Scientific Research under contract No. 2P03B 01324; the Ministry of Science and Technology of the Russian Federation; the Ministry of Education, Science and Sport of the Republic of Slovenia; the National Science Council and the Ministry of Education of Taiwan; and the U.S. Department of Energy.

* on leave from Nova Gorica Polytechnic, Nova Gorica

- [1] S. Eidelman *et al.*, Phys. Lett. B **592**, 1 (2004).
- [2] H. Albrecht *et al.* (ARGUS Collaboration), Phys. Rev. Lett. **56**, 549 (1986).
- [3] H. Albrecht *et al.* (ARGUS Collaboration), Phys. Lett. B **221**, 422 (1989).
- [4] H. Albrecht *et al.* (ARGUS Collaboration), Phys. Lett. B **232**, 398 (1989).
- [5] J. C. Anjos *et al.* (Tagged Photon Spectrometer Collaboration), Phys. Rev. Lett. **62**, 1717 (1989).
- [6] P. Avery *et al.* (CLEO Collaboration), Phys. Rev. D **41**, 774 (1990).
- [7] P. L. Frabetti *et al.* (E687 Collaboration), Phys. Rev. Lett. **72**, 324 (1994).
- [8] P. Avery *et al.* (CLEO Collaboration), Phys. Lett. B **331**, 236 (1994) [Erratum-ibid. B **342**, 453 (1995)].
- [9] T. Bergfeld *et al.* (CLEO Collaboration), Phys. Lett. B **340**, 194 (1994).
- [10] D. Bloch *et al.* (DELPHI Collaboration), CERN-OPEN-2000-015, DELPHI-98-128-CONF-189, Jun 1998. 12pp. 29th International Conference on High-Energy Physics, Vancouver, Canada, 23-29 Jul 1998.
- [11] D. Bloch *et al.* (DELPHI Collaboration), DELPHI-2000-106-CONF 405.
- [12] D. Buskulic *et al.* (ALEPH Collaboration), Z. Phys. C **73**, 601 (1997).
- [13] N. Isgur and M.B. Wise, Phys. Rev. Lett. **66**, 1130 (1991).
- [14] J.L. Rosner, Comm. Nucl. Part. Phys. **16**, 109 (1986).
- [15] S. Godfrey and R. Kokoski, Phys. Rev. D **43**, 1679 (1991).
- [16] A.F. Falk and M.E. Peskin, Phys. Rev. D **49**, 3320 (1994).
- [17] K.Abe *et al.* (Belle Collaboration), Phys. Rev. D **69**, 112002 (2004).
- [18] A. Abashian *et al.* (Belle Collaboration), Nucl. Instr. and Meth. A **479**, 117 (2002).
- [19] Events are generated with a modified version of the CLEO group's QQ program (<http://www.lns.cornell.edu/public/CLEO/soft/qq>); the detector response is simulated using GEANT, R.Brun *et al.*, GEANT 3.21, CERN Report DD/EE/84-1, 1984.
- [20] E. Nakano (Belle Collaboration), Nucl. Instr. and Meth. A **494**, 402 (2002).
- [21] The z coordinate of the track is defined as the z coordinate of the track point closest to the beam in the $r - \phi$ plane. The z axis is opposite the positron beam direction.
- [22] A.Satpathy *et al.* (Belle Collaboration), Phys. Lett. B **553**, 159 (2003).
- [23] G. Brandenburg *et al.* (CLEO Collaboration), Phys. Rev. Lett. **80**, 2762 (1998).
- [24] Eric W. Vaandering (FOCUS Collaboration), Jun 2004. 5pp. To appear in the proceedings of 39th Rencontres de Moriond on QCD and High-Energy Hadronic Interactions, La Thuile, Italy, 28 Mar - 4 Apr 2004. e-Print Archive: hep-ex/0406044.
- [25] N. Uraltsev, Phys. Lett. B **501**, 86 (2001).
- [26] A. Le Yaouanc *et al.*, Phys. Lett. B **520**, 25 (2001).
- [27] J. Blatt and V. Weisskopf, Theoretical Nuclear Physics, p.361, New York: John Wiley & Sons (1952).